

Response to referee Adam Hitchcock (D. S. Macholdt et al., Artifacts from manganese reduction in rock samples prepared by focused ion beam (FIB) slicing for X-ray microspectroscopic analysis)

We appreciate the very thorough and helpful comments by Adam Hitchcock, which have been considered carefully and helped to improve the quality of our manuscript. The referees' comments and our responses are outlined in detail below:

[1.1] Referee comment: The authors interpret the results as evidence that the FIB is drastically alters the Mn oxidation state, which is quite plausible since metal ion reduction by FIB is known from other work. However, the conclusion is not really supported by the data. The evidence, as presented, suggests the thicker regions in the sample have lower amounts of Mn(2+), but there really is not very strong evidence for the presence of Mn(4+) (green in Fig 3), except in some very localized spots. Similarly, the areas identified as Mn(2+) (blue in Fig 3) are localized in a line across the sample, whereas, if the reduction was due to FIB beam damage, then I would expect a more broad distribution of Mn(2+) signal, more like the Mn(3+) distribution (red in fig. 3) reported by the authors. One way to make a more convincing argument would be to use the authors' favourite method to estimate the fraction of Mn(2+), Mn(3+) and Mn(4+) at each pixel in the thinner area they say is not affected by absorption saturation, and also to estimate the thickness of each pixel (for example, from the average STXM image below the onset of the Mn2p edge). A plot of the fraction of each Mn oxidation state as a function of thickness (with suitable binning to improve statistics) should then directly reveal any (anti)-correlation of Mn(2+) amount with thickness. A second way would be to do that type of thickness-oxidation state correlation on several other samples the authors say they have made by FIB and analysed by STXM.

Author Response:

The worthwhile ideas towards a clearer representation of our data gave us the occasion to extensively rework our results and apply a sample thickness normalization routine prior to the spectral clustering. Furthermore, we increased the number of discussed samples to four to provide more (statistical) weight to our argumentation. In addition, results from a total of thirteen samples have been summarized in Table 1. We explain our newly developed sample analysis procedure in the reworked sections below:

“2.2 STXM-NEXAFS measurements and data analysis

[...] To analyze the spatial distribution of different Mn oxidation states in the FIB slices, the STXM image stacks were analyzed by a k-means cluster analysis with Euclidian distances. The analysis sequence included the following specific steps:

1. A careful alignment of the images in the stack was conducted with the help of a custom-made alignment tool.

2. For the subsequent analysis steps, the energy range was limited in MANTiS from 630 to 665 eV, which covers the Mn L<sub>3,2</sub> absorption edge. Note that in the plots of this study the energy range from 631 to 664 eV is shown.
3. According to Beer-Lambert's law:

$$OD(E) = -\ln\left(\frac{I(E)}{I_0(E)}\right) = \mu(E)\rho d \quad (\text{eq. 1})$$

with E = X-ray photon energy, OD(E) = optical density of varnish sample at given E, I(E) = photon flux at given E through the sample, I<sub>0</sub>(E) = incident photon flux at given E through a sample-free region, μ(E) = energy-dependent mass absorption coefficient (see Henke et al., 1993), ρ = density of absorbing atoms in the sample, and d = sample thickness. The background I<sub>0</sub>(E) spectrum was determined to convert the entire stack data into OD(E). A modified version of the histogram-based background selection routine in MANTiS was used here.

4. An OD filter was applied to exclude pixels with OD > 2.5 from the analysis, which are well outside the linear regime of Beer-Lambert's law.
5. For every pixel, the Mn pre-edge value OD<sub>pre</sub> (averaged between 630 and 636 eV) was subtracted from the pixel-specific spectrum. Depending on the energy resolution of the stacks, data from 3 to 20 images was averaged here.
6. For every pixel, the step function-like absorption edge was subtracted from the spectral signature. The generalized logistic function, also known as Richards' curve (Richards, 1959), has been used:

$$OD(E)_{no-edge} = OD(E) + \frac{OD_{post}}{[1 + \exp(-OD(E) + 0.5 \cdot OD_{post})]^{1/(25 \cdot OD(E))}} \quad (\text{eq. 2})$$

with OD(E)<sub>no-edge</sub> = optical density of varnish sample at given E after subtraction of the absorption edge OD from OD(E), here represented by a logistic function, and OD<sub>post</sub> = optical density at Mn post edge, averaged between 660 and 665 eV. The pre-factor 0.5 ensures that the inflection point of the curve is located at half of the edge height. The pre-factor 25 determines the steepness and symmetry of the curve. This value was found empirically and worked well for the current application. Note that without prior subtraction of OD<sub>pre</sub> (step 5), the following modified version of the equation 2 would be relevant:

$$OD(E)_{new} = OD(E) - OD_{pre} + \frac{OD_{post} - OD_{pre}}{[1 + \exp(-OD(E) + 0.5 \cdot OD_{post})]^{1/(2.5 \cdot OD(E))}} \quad (\text{eq. 3})$$

7. After the preprocessing steps 1 to 4, as well as normalization steps 5 and 6, the pixels were pre-classified by means of principle component analysis (PCA) as implemented in MANTiS.
8. With the PCA results as start values, the MANTiS k-means cluster analysis was applied. For the current analysis  $k = 4$  was chosen since it represents the smallest  $k$  that still covers the observed spectral variability in the samples. Within MANTiS the “reduce thickness effect” box was checked to exclude the first PCA component in the subsequent cluster analysis (Lerotic et al., 2004), which is roughly equal to the total Mn absorption per pixel in the observed energy range. The normalization steps 5 and 6 in combination with exclusion of PCA component  $s = 1$  ensure that the cluster analysis partitions the pixel-spectra neither by physical thickness of the FIB slice nor by the heterogeneities in Mn distribution and  $\rho\text{Mn}$ , but only by the spectral patterns at the Mn  $L_{3,2}$  edge, which can be related to Mn oxidation states (Gilbert et al., 2003).

For the further analysis steps beyond the cluster analysis, the non-negative matrix approximation (NNMA) routine, as implemented in MANTiS, was used to extract spectral features while constraining the weightings to be non-negative (for details see Mak et al., 2014). In this work, the NNMA allowed obtaining relative fractions of  $\text{Mn}^{2+}$  and  $\text{Mn}^{4+}$  in every pixel of the stack. Within the MANTiS NNMA routine, we used the following settings: cluster analysis output ( $k = 4$ ) as input for NNMA, spectra similarity = 15, smoothness = 0, sparseness = 0.05, iterations = 500.

### 3 Results and discussion

The SEM overview images and STXM Mn maps in Fig. 1, which illustrate the coating thickness, morphology, and heterogeneity of the selected varnish samples, provide the context for the regions of interest that were analyzed spectroscopically (Fig. 2). The FIB slices were prepared with a wedge-like shape as illustrated in Fig. 1A<sub>2</sub> and 1B<sub>2</sub>. Dedicated SEM measurements with a perpendicular view on the tip of the wedge showed that the thinnest part is  $\sim 100$  nm thick, whereas the thickest part measures  $\sim 1$   $\mu\text{m}$ . For certain samples, part of the wedge was thinned out even further, allowing a comparative analysis of thicker vs. thinner wedges within the same slice (see Fig. 1B<sub>1-3</sub>).

In the course of our STXM-NEXAFS analysis of various varnish samples from different locations worldwide (see Macholdt et al., 2017a), we observed clear indications for beam-related changes in the sample composition. Specifically, differences in the spectral patterns at the Mn  $L_{3,2}$  edge indicate

that a beam-related reduction of the Mn oxyhydroxides has occurred. For the cluster analysis used to discriminate these spectral patterns at the Mn L<sub>3,2</sub> edge – which are a proxy for Mn oxidation states –, it is important to eliminate any influence of the overall sample thickness as well as heterogeneous Mn distributions (e.g., layering) as outlined in Sect. 2.2. As a general trend, low-valence-state Mn species – similar to the Mn<sup>2+</sup> reference spectra – were observed in thinner regions of the FIB wedge, whereas more oxidized Mn species – similar to the Mn<sup>4+</sup> reference spectra – dominate in the thicker regions. Figure 2 emphasizes those samples where the relationship between the optical thickness of the sample and the Mn oxidation state is resolved clearly. The gradient is most obvious in the example shown in Fig. 2D<sub>1-3</sub>. For certain samples, reduced Mn has also been observed around holes within the specimen (e.g., see cracks in Fig. 1D and 2D), which was first interpreted as a sign for reduction of Mn by organics that had previously filled those cavities, especially since some cavities are lined with C-rich material (Macholdt et al., 2015). However, further observations suggest that the reduced Mn in the periphery of the holes can also be explained by a stronger beam exposure in the FIB/SEM preparation. For the sample AR14 Y1 in Fig. 2D<sub>1-3</sub>, we further conducted an NNMA analysis (see Sect. 2.2), which provides a proxy for the relative fractions of Mn<sup>2+</sup> and Mn<sup>4+</sup> in every pixel. This particular sample was chosen because it has the most pixels, thus providing good statistics, and the most homogeneous varnish layer (i.e., no visible clay minerals, low porosity). In Fig. 3, the scatter plots of the obtained Mn<sup>2+</sup> and Mn<sup>4+</sup> fractions against the relative (optical) thickness of the wedge further emphasize the gradients observed in Fig. 2, with highest Mn<sup>2+</sup> fractions in the thinnest and highest Mn<sup>4+</sup> fractions in the thickest part.

The beam-damage-related gradient dominates the oxidation state distribution and, thus, superimposes on the natural heterogeneity in Mn valence states in the varnish. Accordingly, the beam damage fundamentally hampers our original aim to use spatially resolved measurements of the Mn oxidation states for further insights into possible varnish genesis mechanisms. Some indications for layered structures, which may represent residues of the original distribution of Mn valence states, can be seen in Fig. 2A<sub>2</sub> to 2B<sub>2</sub>, however, an interpretation of these structures is highly uncertain. The beam-related Mn reduction has been observed in many samples for which appropriate image stacks were recorded. Table 1 specifies whether a beam-damage effect was found in the analyzed samples and relates the samples to the varnish classification scheme, discriminating five varnish types, proposed by Macholdt et al. (2017a). According to this scheme, three of the samples in Fig. 2 (i.e., AR14 J1, AR14 Y1, and SA14 DV09a) belong to the arid desert varnish type I, whereas one sample (i.e., SA10 #9) belongs to the semi-arid desert varnish type III. Multiple type I and type III samples confirm the

observed trend. For statements on the varnish types II, IV, and V, however, our experimental basis is sparse: No STXM-NEXAFS data is available for type II varnish samples. For type IV and V, STXM stacks have been recorded, however, the varnish coatings of the analyzed samples were too thin to identify clear gradients.“

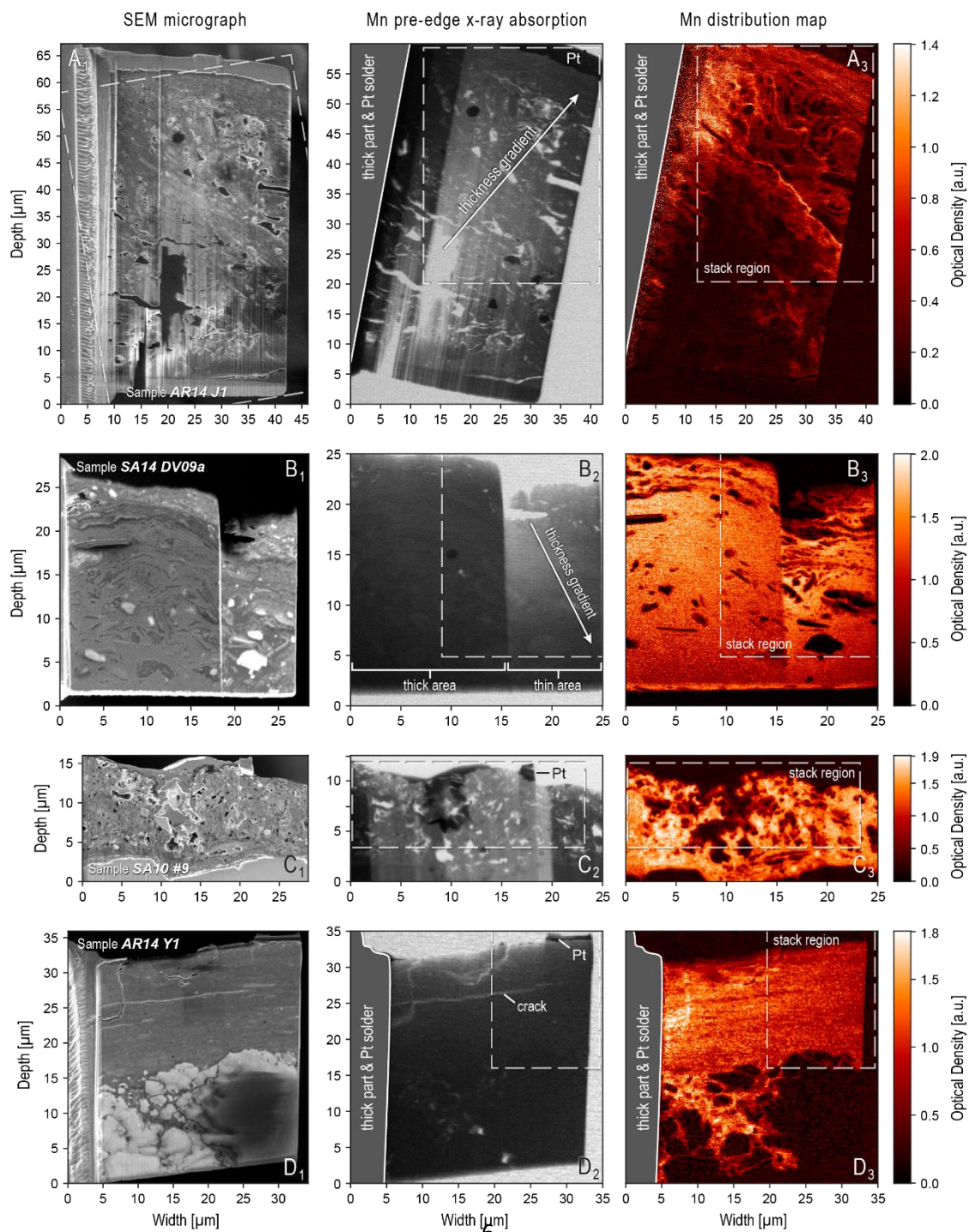


**Fig. 1:** SEM images (**A<sub>1</sub>-D<sub>1</sub>**), Mn pre-edge STXM images (**A<sub>2</sub>-D<sub>2</sub>**), and Mn STXM maps (**A<sub>3</sub>-D<sub>3</sub>**) of FIslices of the rock varnish samples AR14 J1 (**A<sub>1,3</sub>**), SA14 DV09a (**B<sub>1,3</sub>**), SA10 #9 (**C<sub>1,3</sub>**), and AR14 Y1 (**D<sub>1,3</sub>**). All samples are oriented such that the sample support with the Pt solder is on the left side and the rock surface at the top. The varnish layer is visible in the upper part of the images and the bedrock in the lower part in panels C and D. In panels A and B, the Mn-rich varnish layer spans across the whole FIB slice. The luminance values represent transmittance and are to some degree proportional to the sample thickness. Although this is only true for a homogeneous sample, differences in thickness due to the sample preparation and the curtaining effect are obvious and, in some cases, indicated by arrows pointing towards thicker areas, or via brackets in column two. The Mn spectra shown in Fig. 2 were collected within the dashed regions highlighted as ‘stack region’ in column two and three. The Mn pre-edge images were obtained at 635 eV photon energy. The Mn maps were calculated from single images at 635 eV (pre-edge) and 643 eV (on-edge) photon energy.

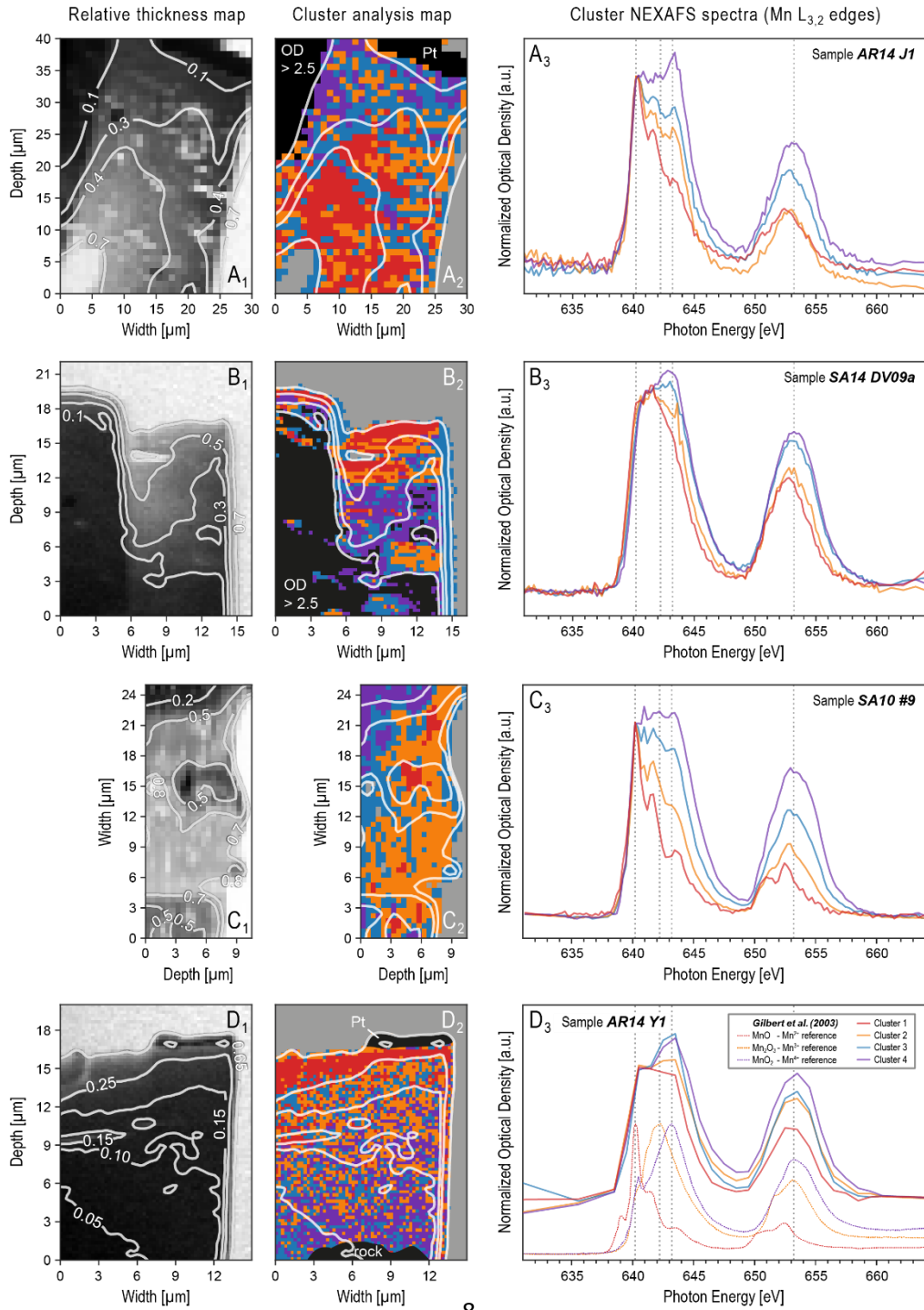


**Fig. 2:** Results from *k*-means cluster analysis applied to STXM image stacks of four different varnish samples, showing influence of beam damage (i.e., reduction of Mn oxyhydroxides) as a function of FIB slice thickness. For background information on the selected varnish samples AR14 J1, SA14 DV09a, SA10 #9, and AR14 Y1 refer to Macholdt et al. (2017a). Panels **A**<sub>1</sub> to **D**<sub>1</sub> show relative optical thickness maps obtained by averaging Mn pre-edge images between 630 and 636 eV. Relative optical thickness maps were normalized to a numeric range from 0 to 1 (0 = lowest transmission in observed area; 1 = full transmission). White contour lines have been calculated based on relative optical thickness maps. Panels **A**<sub>2</sub> to **D**<sub>2</sub> show spatial distribution of pixels across FIB slices partitioned into four clusters based on pixel-specific spectral patterns at the Mn L<sub>3,2</sub> absorption edge. White contour lines project relative optical thicknesses at the Mn pre-edge onto cluster maps. Black regions represent filtered pixels with OD > 2.5, bedrock and Pt. Grey regions represent background pixels. Panels **A**<sub>3</sub> to **D**<sub>3</sub> show corresponding spectra from clustering (same cluster colors in **A**<sub>2</sub> to **D**<sub>2</sub> in **A**<sub>3</sub> to **D**<sub>3</sub>). Reference spectra for Mn<sup>2+</sup>, Mn<sup>3+</sup> and Mn<sup>4+</sup> obtained from Gilbert et al. (2003) are shown in **D**<sub>3</sub>. The spectral pattern of cluster 1 (red) corresponds to the most reduced Mn species – similar to Mn<sup>2+</sup> – and is located mostly in thinnest parts of FIB slices. The spectral pattern of cluster 4 (purple) corresponds to the most oxidized Mn species – similar to Mn<sup>4+</sup> – and is located mostly in the thickest parts of the FIB slices. Clusters 2 (yellow) and 3 (cyan) represent intermediate states.

5

**Table 1.** Overview of all varnish samples analyzed with appropriate STXM-NEXAFS stacks as well as with specification if beam-related Mn reduction has been observed. Samples are grouped according to classification scheme by Macholdt et al. (2017a): type I = arid desert varnish, type II = semi-arid desert varnish, type III = semi-arid desert varnish, type IV = urban area varnish, type V = river splash zone varnish.

Sample name <sup>1</sup>	Varnish type	Beam damage-related Mn reduction observed:	Comment
AR14 J1 (AR-J)	I	Yes, clearly	Refer to Fig. 1 & 2
AR14 Y1 (AR-Y)	I	Yes, clearly	Refer to Fig. 1, 2 & 3
CA14 DV11 (CA-DV)	I	Unknown	Spectral gradient overlaps with porous regions, dominant varnish/rock boundary zone
CA14 JC8 (CA-JC)	I	Yes, clearly	--
IS13 V1 (IS)	I	Unknown	Low spectral quality & varnish coating too narrow
IS13 V3 (IS)	I	Unknown	If yes, superimposed by sample layering
--	II	--	No STXM-NEXAFS data for type II available
SA10 #9 (SA-1)	III	Yes, clearly	Refer to Fig. 1 & 2
SA13 mM-f (SA-1)	III	Unknown	Sample too thick in most parts, remaining pixels indicate rather a random species distribution
SA14 DV09a (SA-2)	III	Yes, clearly	Refer to Fig. 1 & 2
SA14 DV09b (SA-2)	III	Yes, but uncertain	Sample too thick in most parts & low statistics
SC	IV	Unknown	Varnish coating too narrow to resolve gradients
FM	IV	Unknown	Varnish coating too narrow to resolve gradients
E Canal	V	Unknown	Varnish coating too narrow to resolve gradients

<sup>1</sup> Sample names kept consistent with Table 1 in Macholdt et al. (2017a)

As suggested, the (anti-)correlation of Manganese species with thickness was exemplarily done for one sample:

“[...] For the sample AR14 Y1 in Fig. 2D<sub>1-3</sub>, we further conducted an NNMA analysis (see Sect. 2.2), which provides a proxy for the relative fractions of Mn<sup>2+</sup> and Mn<sup>4+</sup> in every pixel. This particular sample was chosen because it has the most pixels, thus providing good statistics, and the most homogeneous varnish layer (i.e., no visible clay minerals, low porosity). In Fig. 3, the scatter plots of the obtained Mn<sup>2+</sup> and Mn<sup>4+</sup> fractions against the relative (optical) thickness of the wedge further emphasize the gradients observed in Fig. 2, with highest Mn<sup>2+</sup> fractions in the thinnest and highest Mn<sup>4+</sup> fractions in the thickest part. [...]

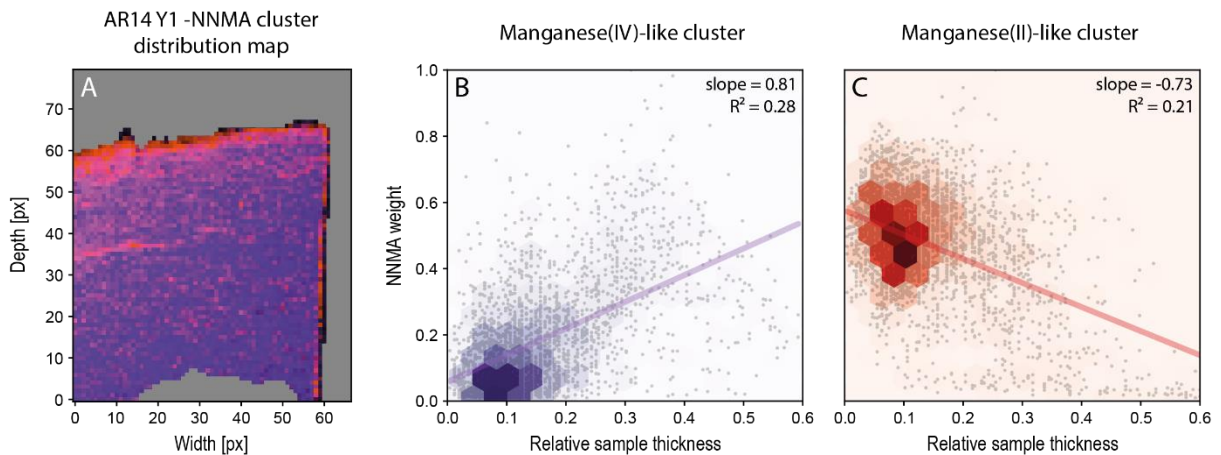


**Fig. 3:** Non-negative matrix approximation (NNMA) of sample AR14 Y1. Panel A shows the spatial distribution of the Mn<sup>2+</sup>-associated (most reduced) cluster (red) and the Mn<sup>4+</sup>-associated (most oxidized) cluster (violet). Panels B and C show the pixel weights from the NNMA analysis of each cluster against the “relative thickness” represented by the Mn pre-edge luminance values, scaled from 1 to 0, where 0 represents full transmission and 1 stands for the darkest pixel in the observed area. Thick areas with relative thickness > 0.6 were masked, as well as non-varnish regions (background, Pt or rock). Compare with Fig. 1D and Fig. 2D. There is a positive correlation with thickness for the more oxidized cluster and an anti-correlation for the more reduced cluster. Linear fits along with their slopes and R<sup>2</sup>-values are shown to emphasize the observed trend. Very striking is the increased weight of Mn<sup>2+</sup>-like pixels in thin regions at the top, along the crack (compare with Fig. 1 D<sub>2</sub>) and along the outer cutting line (right side).”

[1.2] Referee comment: (p2 27) ‘phosphor screen;’ – change to ‘phosphor coating – screen implies imaging but only a single number is read from the detector at each pixel in a STXM image.

[1.3] Referee comment: (p2, 27) ‘generated visible’ → ‘generated burst of visible’ – it is not individual visible photons, but bursts since there is ~1 visible photon per ~3 eV of photon energy

Author Response: To make the introduction more concise, we deleted the general information on STXM, since the details are well documented in the references we are listing in the newly rephrased paragraph:

“In view of the controversy regarding the varnish genesis and the scarcity of information on the varnish microchemistry, we conducted STXM-NEXAFS measurements to investigate element distributions within the varnish coatings, along with spectroscopic information on the elements’ binding environments and oxidation states. Experimental details on STXM-NEXAFS can be found in Kilcoyne et al. (2003) and Moffet et al. (2011).”

[1.4] Referee comment: (p3, 16) to a few hundred degrees - is this proven or speculation ? reference ? would it be worth to compare FIB of RT and heated varnish samples ? – if the heat during FIB is important, a change in degree of radiation damage might occur. (cryo-FIB is known to reduce damage).

Author Response: Regarding this valuable comment, we re-evaluated the damaging potential of sample heating from SEM and FIB, added some quantitative information, and rephrased essential parts of the introduction:

“[...] The amorphization coincides with heating of the outer sample surface in the course of the collision cascade (Volkert and Minor, 2007; Fischione et al., 2017) along with the occurrence of so-called “thermal spikes”, which can easily reach a few thousand Kelvin (Ovchinnikov et al., 2015). Because of the immediate vaporization of the affected volume within  $10^{-12}$  s (Ovchinnikov et al., 2015), the thermal effect on the bulk material is rather low. For samples with both, good thermal conductivity and good thermal connection, ion beam heating plays a negligible role in the bulk (Volkert and Minor, 2007), but for materials with inefficient heat dissipation (e.g., due to a low thermal conductivity, such as in SiO<sub>2</sub>) a temperature increase up to 500 °C was calculated (Ishitani and Kaga, 1995). If samples are very thin, even in metals, temperatures up to 370 °C (Kim and Carpenter, 1987) or even >400 °C (Cen and Van Benthem, 2018) can be reached. This is especially destructive for organic samples, such as polymers, which tend to melt and decompose under common FIB conditions (Volkert and Minor; 2007, Schmied et al., 2014) . For instance, a temperature rise of 171 °C has been observed by Bassim et al. (2012) for polyacrylamide. During thinning with rather low beam currents of 0.23 nA, a temperature rise to above the melting temperature of Crystalbond™ 509 (121 °C) has been observed by Li and Liu (2017). This heating can be reduced to a large extent with optimized scanning patterns (Schmied, 2014) or simply by cooling the sample (Fischione et al., 2017). The susceptibility for beam damage and the thickness of the amorphous layer strongly depends on the type of ion and the sputtered material. The damaged layer thickness typically ranges from a few to a few tens of nanometers (Mayer et al., 2007; Mikmekova et al., 2011). Sample heating also facilitates the occurrence of uncommon types of beam damage, such as preferential sputtering (Volkert and Minor, 2007), which occurs in materials with more than one atom species, especially if the compound can decompose chemically. In-depth information on sample heating (Kim and Carpenter, 1987; Cen and Van Benthem, 2018; Volkert and Minor, 2007; Ovchinnikov et al., 2015; Ishitani and Kaga, 1995), beam damage (Gutierrez-Urrutia, 2017; Mayer et al., 2007; Betz and Wehner, 1983; Prenitzer et al., 2003) and experimental reduction strategies of these effects (Bassim et al., 2012; Barber, 1993) can be found in the cited literature. [...]

As radiolysis shows a temperature dependence, its damaging potential can be minimized when the irradiated specimens are cooled (Pantano and Madey, 1981; Egerton et al., 2004; Egerton, 2012). This should not lead to the false conclusion that sample heating due to the electron beam is as significant as with ions. The temperature rise through electron exposure is not expected to exceed a few Kelvin (Tokunaga et al., 2012; Holmes et al., 2000; Hoffman and Paterson, 1996).”

In our concluding remarks, we now explicitly link sample heating to the observed radiation damage and listed cryo-FIB, among other methods, as a possible approach to minimize beam damage:

“[...] For instance, Fondell et al. (2018) report that sputter reduction of maghemite is similar to heat treatment of the sample in vacuum. The dissociation of carbonates (Christie et al., 1981) and sulfates (Contarini and Rabalais, 1985) has been observed and attributed to a combination of thermal sputtering connected to thermal spikes and electron sputtering. Momentum transfer alone (preferential sputtering due to mass differences) could not explain the observed reactions. A follow-up study on previously heated samples could therefore help to better understand the potential thermal decomposition of rock varnish. [...]

If available, a cryo-FIB approach (Bassim et al. 2012) could be applied. Sezen et al. (2011) showed, however, that cryogenic conditions could not prevent or even slow down the degradation of conjugated polymers during FIB milling. [...]

[1.5] Referee comment: (p 4 ,14) the metal coating is done, in part to reduce damage from heating or charging. Was there any study of the dependence on the amount of damage on the thickness of the Pt coating ?

Author Response: The application of the Pt stripe is an integral part of the FIB preparation procedure and a consistently thick coating was applied to all samples to keep them comparable. The ablation of the Pt strip was also used as an indicator for a sufficiently thinned FIB slice.

In our data, compare Fig. 2 A<sub>2</sub> and D<sub>2</sub>, we see no damage reducing effect due to the Pt stripe’s improved heat dissipation. However, it would be interesting to test this assumption on a FIB sample without a Pt stripe. We also rephrased the sentence to which the question refers:

“The Pt stripe acts as a mask to reduce damage from perpendicular ion collisions on the sample surface throughout the subsequent milling steps.”

[1.6] Referee comment: (p 6, 23) ‘main absorption edges at different energies’ → it would be useful to define what you mean by ‘edges’. I suspect the XPS peak energies for Mn(2+/3+/4+). As you note, the spectra of each ox state (in fact each ‘compound’ or local environment) are characterized by multiple peaks, and a single ‘energy’, ‘edge (in XAS sense)’ or ‘peak’ is not enough to uniquely identify oxidation state. It is the overall pattern that is needed. This should be brought out.

Author Response: True. See response to [1.8].

[1.7] Referee comment: (p 6, 25) connecting multiplets to oxidation state is actually a gross simplification. Multiplet refers specifically to the [core electron – valence electron] exchange interaction. Oxidation state (interpreted as a net valence electron count) is only indirectly connected.

Author Response: Agree. See response to [1.8].

[1.8] Referee comment: (p 6, 27) “for each oxidation state the absorption at a certain energy (Mn 2+ ~ 639.7 eV, Mn 3+ ~641.35 eV, Mn 4+ ~ 643.05 eV) is predominant, so that the oxidation states can be distinguished from each other” again, I would stress that it is the PATTERN of peaks that is connected to oxidation, not a single peak.

Author Response to [1.6], [1.7], and [1.8]: We agree with the referee that the wording in the corresponding paragraph is confusing. Accordingly, we reworked the original text section

“[...] The Mn L<sub>3</sub> and L<sub>2</sub> absorption edges (short the Mn L<sub>3,2</sub> edge) are located in the energy range from ~635 to ~660 eV (i.e., electron binding energies in elemental Mn: 638.7 eV at L<sub>3</sub> and 649.9 eV at L<sub>2</sub> according to Fuggle and Mårtensson, 1980). The L<sub>3</sub> and L<sub>2</sub> edges consist of multiplets of peaks, which reflect the density of unoccupied 3d states (Gilbert et al., 2003). It is well documented in the literature that the NEXAFS spectra show different spectral patterns for the oxidation states Mn<sup>2+</sup>, Mn<sup>3+</sup>, and Mn<sup>4+</sup> (Cramer et al., 1991, Pecher et al., 2003, Gilbert et al., 2003, Nesbitt and Banerjee, 1998) and that the ratio of the L<sub>3</sub> and L<sub>2</sub> edge intensities can be taken as a measure for the 3d occupancy and thus for the valence state (Cramer et al., 1991, Kurata and Colliex, 1993). The energies of the most intense peaks within the L<sub>3</sub> multiplets for the individual oxidation states are the following: Mn<sup>2+</sup> ~ 640.2 eV, Mn<sup>3+</sup> ~ 642.2 eV, Mn<sup>4+</sup> ~ 643.2 eV (Gilbert et al., 2003).”

and added a few words of explanation to the ‘results and discussion’ section:

“Specifically, differences in the spectral patterns at the Mn L<sub>3,2</sub> edge indicate that a beam-related reduction of the Mn oxyhydroxides has occurred. For the cluster analysis used to discriminate these spectral patterns at the Mn L<sub>3,2</sub> edge – which are a proxy for Mn oxidation states –, it is important to eliminate any influence of the overall sample thickness as well as heterogeneous Mn distributions (e.g., layering) as outlined in Sect. 2.2.”

[1.9] Referee comment: (p 7, caption to Fig 2) The caption calls (c) and (e) “images”, but they are not – they are color coded cluster signal distributions.

Author Response: Thank you for pointing this out. We clarified this in the new caption of Fig. 2:

“Panels **A**<sub>2</sub> to **D**<sub>2</sub> show spatial distribution of pixels across FIB slices partitioned into four clusters based on pixel-specific spectral patterns at the Mn L<sub>3,2</sub> absorption edge.”

[1.10] Referee comment: (p 8, 31) ‘While STXM-NEXAFS measurements are conducted with energies in the eV range, FIB preparation and SEM imaging utilize energies in the keV range.’ The correlation of damage-potential and particle energy is an oversimplification. The X-rays transfer ALL their energy to the sample on absorption, whereas the ion and electron beams transfer only a portion. For ions it is momentum rather than energy transfer that is important I suspect. The reduction is probably done by liberated electrons.

Author Response: The paragraph referred to has been reworked to point out the very different energy transfer processes:

“Generally, the varnish samples experienced an intense ion and electron bombardment as well as high X-ray exposure in the course of the preparation and analysis. Accordingly, all applied techniques – FIB, SEM, and STXM – are in principle potential sources for the beam damage (Süzer 2000, Bassim et al. 2012). The soft X-rays in STXM (~0.3 to 0.7 keV), accelerated electrons in SEM (~2 to 5 keV), and accelerated Ga<sup>+</sup> ions in FIB (~30 kV) are characterized by widely different energies. Moreover, their energies – and thus the potential damage – are deposited in the samples via different mechanistic pathways: Soft X-rays mostly act via core electron excitation up to an ionization of the atom, followed by a relaxation and filling of the core hole vacancy with associated photon and Auger electron emissions. As stated in the introduction, accelerated electrons mostly interact with varnish-like specimens via inelastic scattering, possibly causing radiolytic processes in the course of electronic excitations. Accelerated ions mostly act via nuclear, i.e. elastic collisions, resulting in sputtering, but electronic excitations should not be neglected. Our experiments showed, however, that the damaging effect of STXM is negligible: In dedicated tests, sequences of successive stack scans were recorded on the same area and no difference in the spectral patterns (i.e., at the absorption edges of Mn and other elements) could be observed. Moreover, previous X-ray microspectroscopy measurements have been successfully performed on materials with different Mn oxidation states (e.g., Bargar et al., 2001, Glasauer et al., 2006, Pecher et al., 2000, Pecher et al., 2003, Tebo et al., 2004, Toner et al., 2005).“

All changes requested and/or recommended by the referee in his minor comments have been implemented in the revised version of the manuscript.

## References:

- Barber, D. J.: Radiation damage in ion-milled specimens: characteristics, effects and methods of damage limitation, *Ultramicroscopy*, 52(1), 101–125, doi:10.1016/0304-3991(93)90025-S, 1993.
- Bargar, J., Tebo, B., K., P., McCubbery, D., Chiu, V. and B., T.: Manganese Oxide Biomineralization by Spores of the Marine *Bacillus* sp. Strain SG-1, in AGU Fall Meeting Abstracts., 2001.
- Bassim, N. D., De Gregorio, B. T., Kilcoyne, A. L. D., Scott, K., Chou, T., Wirick, S., Cody, G. and Stroud, R. M.: Minimizing damage during FIB sample preparation of soft materials, *J. Microsc.*, 245(3), 288–301, doi:10.1111/j.1365-2818.2011.03570.x, 2012.
- Betz, G. and Wehner, G. K.: Sputtering of multicomponent materials, in *Sputtering by Particle Bombardment II*, Topics in Applied Physics, vol 52., edited by R. Behrish, pp. 11–90, Springer Berlin, Heidelberg., 1983.
- Cen, X. and van Benthem, K.: Ion beam heating of kinetically constrained nanomaterials, *Ultramicroscopy*, 186, 30–34, doi:10.1016/j.ultramic.2017.12.005, 2018.
- Christie, A., Sutherland, I. and Walls, J.: An XPS study of ion-induced dissociation on metal carbonate surfaces, *Vacuum*, 31(10–12), 513–517, doi:10.1016/0042-207X(81)90051-8, 1981.
- Contarini, S. and Rabalais, J. W.: Ion bombardment-induced decomposition of Li and Ba sulfates and carbonates studied by X-ray photoelectron spectroscopy, *J. Electron Spectros. Relat. Phenomena*, 35(2), 191–201, doi:10.1016/0368-2048(85)80056-6, 1985.
- Cramer, S. P., DeGroot, F. M. F., Ma, Y., Chen, C. T., Sette, F., Kipke, C. A., Eichhorn, D. M., Chan, M. K. and Armstrong, W. H.: Ligand field strengths and oxidation states from manganese L-edge spectroscopy, *J. Am. Chem. Soc.*, 113(21), 7937–7940, doi:10.1021/ja00021a018, 1991.
- Egerton, R. F.: Mechanisms of radiation damage in beam-sensitive specimens, for TEM accelerating voltages between 10 and 300 kV, *Microsc. Res. Tech.*, 75(11), 1550–1556, doi:10.1002/jemt.22099, 2012.
- Egerton, R. F., Li, P. and Malac, M.: Radiation damage in the TEM and SEM, *Micron*, 35(6), 399–409, doi:10.1016/j.micron.2004.02.003, 2004.
- Fischione, P. E., Williams, R. E. A., Genç, A., Fraser, H. L., Dunin-Borkowski, R. E., Luysberg, M., Bonifacio, C. S. and Kovács, A.: A Small Spot, Inert Gas, Ion Milling Process as a Complementary Technique to Focused Ion Beam Specimen Preparation, *Microsc. Microanal.*, 23(4), 782–793, doi:10.1017/S1431927617000514, 2017.
- Fondell, M., Gorgoi, M., Boman, M. and Lindblad, A.: Surface modification of iron oxides by ion bombardment – Comparing depth profiling by HAXPES and Ar ion sputtering, *J. Electron Spectros. Relat. Phenomena*, 224, 23–26, doi:10.1016/j.elspec.2017.09.008, 2018.
- Fuggle, J. C. and Mårtensson, N.: Core-level binding energies in metals, *J. Electron Spectros. Relat. Phenomena*, 21(3), 275–281, doi:10.1016/0368-2048(80)85056-0, 1980.
- Gilbert, B., Frazer, B. H., Belz, A., Conrad, P. G., Neelson, K. H., Haskel, D., Lang, J. C., Srajer, G. and De Stasio, G.: Multiple Scattering Calculations of Bonding and X-ray Absorption Spectroscopy of Manganese Oxides, *J. Phys. Chem. A*, 107(16), 2839–2847, doi:10.1021/jp021493s, 2003.

- Glasauer, S. M., Langley, S., Beveridge, T. J., Fakra, S., Tyliczszak, T., Shuh, D., Boyanov, M. and Kemner, K.: The Internalization of Iron and Manganese as Discrete Particles During the Bioreduction of Fe(III) and Mn(IV) by a Dissimilatory Metal-Reducing Bacterium, AGU Fall Meet. Abstr., B13B–1095, 2006.
- Gutierrez-Urrutia, I.: Analysis of FIB-induced damage by electron channelling contrast imaging in the SEM, *J. Microsc.*, 265(1), 51–59, doi:10.1111/jmi.12462, 2017.
- Henke, B. L., Gullikson, E. M. and Davis, J. C.: X-Ray Interactions: Photoabsorption, Scattering, Transmission, and Reflection at  $E = 50\text{--}30,000$  eV,  $Z = 1\text{--}92$ , *At. Data Nucl. Data Tables*, 54(2), 181–342, doi:10.1006/adnd.1993.1013, 1993.
- Hoffman, A. and Paterson, P. J. K.: Electron stimulated reduction of sapphire studied by electron energy loss and Auger spectroscopies, *Surf. Sci.*, 352–354, 993–997, doi:10.1016/0039-6028(95)01314-8, 1996.
- Holmes, J. L., Bachus, K. N. and Bloebaum, R. D.: Thermal effects of the electron beam and implications of surface damage in the analysis of bone tissue, *Scanning*, 22(4), 243–248, doi:10.1002/sca.4950220403, 2006.
- Ishitani, T. and Kaga, H.: Calculation of Local Temperature Rise in Focused-Ion-Beam Sample Preparation, *J. Electron Microsc. (Tokyo)*, 44(5), 331–336, doi:10.1093/oxfordjournals.jmicro.a051185, 1995.
- Kilcoyne, A. L. D., Tyliczszak, T., Steele, W. F., Fakra, S., Hitchcock, P., Franck, K., Anderson, E., Harteneck, B., Rightor, E. G., Mitchell, G. E., Hitchcock, A. P., Yang, L., Warwick, T. and Ade, H.: Interferometer-controlled scanning transmission X-ray microscopes at the Advanced Light Source., *J. Synchrotron Radiat.*, 10(Pt 2), 125–36, Available from: <http://www.ncbi.nlm.nih.gov/pubmed/12606790>, 2003.
- Kim, M. J. and Carpenter, R. W.: Tem specimen heating during ion beam thinning: microstructural instability, *Ultramicroscopy*, 21, 327–334, 1987.
- Kurata, H. and Colliex, C.: Electron-energy-loss core-edge structures in manganese oxides, *Phys. Rev. B*, 48(4), 2102–2108, doi:10.1103/PhysRevB.48.2102, 1993.
- Lerotic, M., Jacobsen, C., Schäfer, T. and Vogt, S.: Cluster analysis of soft X-ray spectromicroscopy data, *Ultramicroscopy*, 100(1–2), 35–57, doi:10.1016/j.ultramic.2004.01.008, 2004.
- Li, J. and Liu, P.: Important Factors to Consider in FIB Milling of Crystalline Materials, in *Characterization of Minerals, Metals, and Materials 2017*, edited by S. Ikhmayies, B. Li, J. S. Carpenter, J. Li, J.-Y. Hwang, S. N. Monteiro, and D. Firrao, pp. 329–336, Springer, Cham., 2017.
- Macholdt, D. S., Jochum, K. P., Pöhlker, C., Stoll, B., Weis, U., Weber, B., Müller, M., Kappl, M., Buhre, S., Kilcoyne, A. L. D., Weigand, M., Scholz, D., Al-Amri, A. M. and Andreae, M. O.: Microanalytical methods for in-situ high-resolution analysis of rock varnish at the micrometer to nanometer scale, *Chem. Geol.*, 411, 57–68, doi:10.1016/j.chemgeo.2015.06.023, 2015.
- Macholdt, D. S., Jochum, K. P., Pöhlker, C., Arangio, A., Förster, J.-D., Stoll, B., Weis, U., Weber, B., Müller, M., Kappl, M., Shiraiwa, M., Kilcoyne, A. L. D., Weigand, M., Scholz, D., Haug, G. H.,

- Al-Amri, A. and Andreae, M. O.: Characterization and differentiation of rock varnish types from different environments by microanalytical techniques, *Chem. Geol.*, 459, 91–118, doi:10.1016/j.chemgeo.2017.04.009, 2017a.
- Mak, R., Lerotic, M., Fleckenstein, H., Vogt, S., Wild, S. M., Leyffer, S., Sheynkin, Y. and Jacobsen, C.: Non-negative matrix analysis for effective feature extraction in X-ray spectromicroscopy, *Faraday Discuss.*, 171, 357–371, doi:10.1039/C4FD00023D, 2014.
- Mayer, J., Giannuzzi, L. A., Kamino, T. and Michael, J.: TEM Sample Preparation and Damage, *MRS Bull.*, 32(5), 400–407, doi:10.1557/mrs2007.63, 2007.
- Mikmeková, S., Matsuda, K., Watanabe, K., Ikeno, S., Müllerová, I. and Ludek, F.: FIB Induced Damage Examined with the Low Energy SEM, *Mater. Trans.*, 52(3), 292–296, doi:10.2320/matertrans.MB201005, 2011.
- Moffet, R. C., Tivanski, A. V. and Gilles, M. K.: Scanning Transmission X-ray Microscopy: Applications in Atmospheric Aerosol Research, in *Fundamentals and Applications in Aerosol Spectroscopy*, edited by R. Signorell and J. Reid, CRC Press., 2011.
- Nesbitt, H. W. and Banerjee, D.: Interpretation of XPS Mn(2p) spectra of Mn oxyhydroxides and constraints on the mechanism of MnO<sub>2</sub> precipitation, *Am. Mineral.*, 83(3–4), 305–315, doi:10.2138/am-1998-3-414, 1998.
- Ovchinnikov, V. V., Makhin'ko, F. F. and Solomonov, V. I.: Thermal-spikes temperature measurement in pure metals under argon ion irradiation (E = 5–15 keV), *J. Phys. Conf. Ser.*, 652(1), 012070, doi:10.1088/1742-6596/652/1/012070, 2015.
- Pantano, C. G. and Madey, T. E.: Electron beam damage in Auger electron spectroscopy, *Appl. Surf. Sci.*, 7(1–2), 115–141, doi:10.1016/0378-5963(81)90065-9, 1981.
- Pecher, K.: Charge state mapping of mixed valent iron and manganese mineral particles using Scanning Transmission X-ray Microscopy (STXM), in *AIP Conference Proceedings*, vol. 507, pp. 291–300, AIP., 2000.
- Pecher, K., McCubbery, D., Kneedler, E., Rothe, J., Bargar, J., Meigs, G., Cox, L., Nealson, K. and Tonner, B.: Quantitative charge state analysis of manganese biominerals in aqueous suspension using scanning transmission X-ray microscopy (STXM), *Geochim. Cosmochim. Acta*, 67(6), 1089–1098, doi:10.1016/S0016-7037(02)01229-2, 2003.
- Prenitzer, B. I., Urbanik-Shannon, C. A., Giannuzzi, L. A., Brown, S. R., Irwin, R. B., Shofner, T. L. and Stevie, F. A.: The Correlation between Ion Beam/Material Interactions and Practical FIB Specimen Preparation, *Microsc. Microanal.*, 9(03), 216–236, doi:10.1017/S1431927603030034, 2003.
- Richards, F. J.: A Flexible Growth Function for Empirical Use, *J. Exp. Bot.*, 10(2), 290–301, doi:10.1093/jxb/10.2.290, 1959.
- Roof, S. and Callagan, C.: The Climate of Death Valley, California, *Bull. Am. Meteorol. Soc.*, 84(12), 1725–1740, doi:10.1175/BAMS-84-12-1725, 2003.
- Schmied, R., Fröch, J. E., Orthacker, A., Hobisch, J., Trimmel, G. and Plank, H.: A combined approach to predict spatial temperature evolution and its consequences during FIB processing of soft matter, *Phys. Chem. Chem. Phys.*, 16(13), 6153–6158, doi:10.1039/c3cp55308f, 2014.

- Sezen, M., Plank, H., Fisslthaler, E., Chernev, B., Zankel, A., Tchernychova, E., Blümel, A., List, E. J. W., Groggera, W. and Pölta, P.: An investigation on focused electron/ion beam induced degradation mechanisms of conjugated polymers, *Phys. Chem. Chem. Phys.*, (13), 20235–20240, doi:10.1039/C1CP22406A, 2011.
- Süzer, Ş.: XPS Investigation of X-Ray-Induced Reduction of Metal Ions, *Appl. Spectrosc.*, 54(11), 1716–1718, doi:10.1366/0003702001948772, 2000.
- Tebo, B. M., Bargar, J. R., Clement, B. G., Dick, G. J., Murray, K. J., Parker, D., Verity, R. and Webb, S. M.: BIOGENIC MANGANESE OXIDES: Properties and Mechanisms of Formation, *Annu. Rev. Earth Planet. Sci.*, 32(1), 287–328, doi:10.1146/annurev.earth.32.101802.120213, 2004.
- Tokunaga, T., Narushima, T., Yonezawa, T., Sudo, T., Okubo, S., Komatsubara, S., Sasaki, K. and Yamamoto, T.: Temperature distributions of electron beam-irradiated samples by scanning electron microscopy., *J. Microsc.*, 248(3), 228–33, doi:10.1111/j.1365-2818.2012.03666.x, 2012.
- Toner, B., Fakra, S., Villalobos, M., Warwick, T. and Sposito, G.: Spatially Resolved Characterization of Biogenic Manganese Oxide Production within a Bacterial Biofilm, *Appl. Environ. Microbiol.*, 71(3), 1300–1310, doi:10.1128/AEM.71.3.1300-1310.2005, 2005.
- Volkert, C. A. and Minor, A. M.: Focused Ion Beam Microscopy and Micromachining, *MRS Bull.*, 32, doi:10.1016/j.arth.2016.01.046, 2007.